Imaging of Calibrated Defects in Additively Manufactured Materials

Pulsed Thermal Tomography Nondestructive Examination of Additively Manufactured Reactor Materials and Components

Nuclear Science and Engineering Division

About Argonne National Laboratory

Argonne is a U.S. Department of Energy laboratory managed by UChicago Argonne, LLC
under contract DE-AC02-06CH11357. The Laboratory's main facility is outside Chicago, at
9700 South Cass Avenue, Argonne, Illinois 60439. For information about Argonne
and its pioneering science and technology programs, see www.anl.gov.

Imaging of Calibrated Defects in Additively Manufactured Materials

Pulsed Thermal Tomography Nondestructive Examination of Additively Manufactured Reactor Materials and Components

prepared by
Alexander Heifetz[1], Xin Zhang[1,2], Jafar Saniie[2], Dmitry Shribak[1,3], Thomas W. Elmer[1], Brian Saboriendo[1,4], Sasan Bakhtiari[1], William Cleary[5]

[1]Nuclear Science Engineering Division, Argonne National Laboratory
[2]Department of Electrical and Computer Engineering, Illinois Institute of Technology, Chicago, IL
[3]Department of Physics, University of Chicago, Chicago, IL
[4]Department of Physics, DePaul University, Chicago, IL
[5]Westinghouse Electric Company, Columbia, SC

March 31, 2020

Table of Contents

List of Figures

Abstract

Additive manufacturing (AM, or 3D printing) for commercial nuclear energy applications is an emerging method for cost-efficient manufacturing aimed at replacing aging nuclear reactor parts and reducing costs for new construction. Known material flaws in AM include low-density regions consisting of non-sintered powder, which have to be detected to ensure the safety of long-term performance nuclear reactor components. Currently, limited options are available for nondestructive evaluation (NDE), either during or post manufacturing. As a solution to NDE of AM, we are developing pulsed thermal imaging which is non-contact, one-sided, and scalable to arbitrary size and shape of the AM parts. Pulsed thermography (PT) system utilizes a high intensity flash lamp to rapidly heat surface of sample, and a high sensitivity fast-frame megapixel infrared (IR) camera to capture data of surface temperature variations. The acquired data cube consists of a stack of surface temperature images taken at different times. Information about material internal defects is extracted by analyzing the data cube.

This report provides results of preliminary performance evaluation of pulsed thermal imaging capability in detection of imprinted flaws in AM metallic structures. The flaws were introduced into AM parts as imprinted hemispherical low density regions, consisting of trapped un-sintered metallic powder. Specimens for developed for this study consisted of AM stainless steel 316 and Inconel 718 plates. The diameters of imprinted defects varied from 1mm to 8mm, and their depths below the plate flat surface varied between 1mm and 6mm.

Pulsed thermal tomography (PTT) processes the measured data cube to obtain 3D reconstructions of material effusivity using a unique inversion algorithm developed at Argonne. PTT has been previously used in imaging of similar size flat bottom hole (FBH) simulated defects in stainless steel 316 and Inconel 718 specimens. In the study involving AM specimens, PTT imaging results have shown that 1mm-diameter defects located 1mm and 2mm below the surface of specimens were detectable. Larger size defects were detectable at greater depth.

We also explored an alternative approach to detection of material flaws in PT data cube, which is using neural learning-based approach to blind source separation. Detection of small material defects requires finding features in the data cube which have signal contrast levels approaching sensitivity limit of IR camera. In this study, an optimized Neural Learning based Blind Source Separation (NLBSS) algorithm, including Principal Component Analysis (PCA), and Independent Component Analysis (ICA) is demonstrated to automatically extract principal temporal and spatial features of thermography frames to enhance flaw detection. By using the NLBSS algorithm, material internal defects can be automatically detected. Furthermore, this processing approach compensates for experimental thermal imaging artifacts, such as noise and uneven heating. By merging artificial intelligence with phtotothermics, the NDE system detects internal calibrated defects of various sizes and depths in AM nuclear-grade metallic alloys.

1. Introduction

Additive manufacturing (AM) for nuclear energy applications is an emerging method for cost-efficient manufacturing aimed at replacing aging nuclear reactor parts and reducing costs for new construction of advanced reactors [1,2]. In addition, AM However, there are still challenges for widespread deployment of AM in nuclear reactors, particular the ability to perform nondestructive evaluation (NDE) of AM parts. Because of the intrinsic features of AM process for fabricating stainless steel and nickel super alloys metallic parts, such as selective laser melting (SLM), defects can appear consisting of low density regions or pores. Figure 1 provides a schematic visualization of the SLM process. In Step 1, the system prepares the powder bed for fabrication. Step 2 consists of selective melting and fusing of powder particles. Porosity can be introduced into AM parts due to incomplete melting of the powder particles or insufficient overlapping of the melt pools [3]. Oscillations in the surface of the melt pool caused by rapid heating and cooling result in powder ejection and splattering of the melt, resulting in surface roughness and porosity [4]. Furthermore, improper cooling rates can cause the formation of non-equilibrium phases and residual stresses, requiring post-process heat treatments [5-7]. The pore is potentially a seed for crack formation in the structure due to non-uniform expansion of the material in response to thermal and mechanical stresses in nuclear reactor [8,9]. Pores have been observed in destructive examinations to be on the order of 20µm and larger.

(a)   (b)
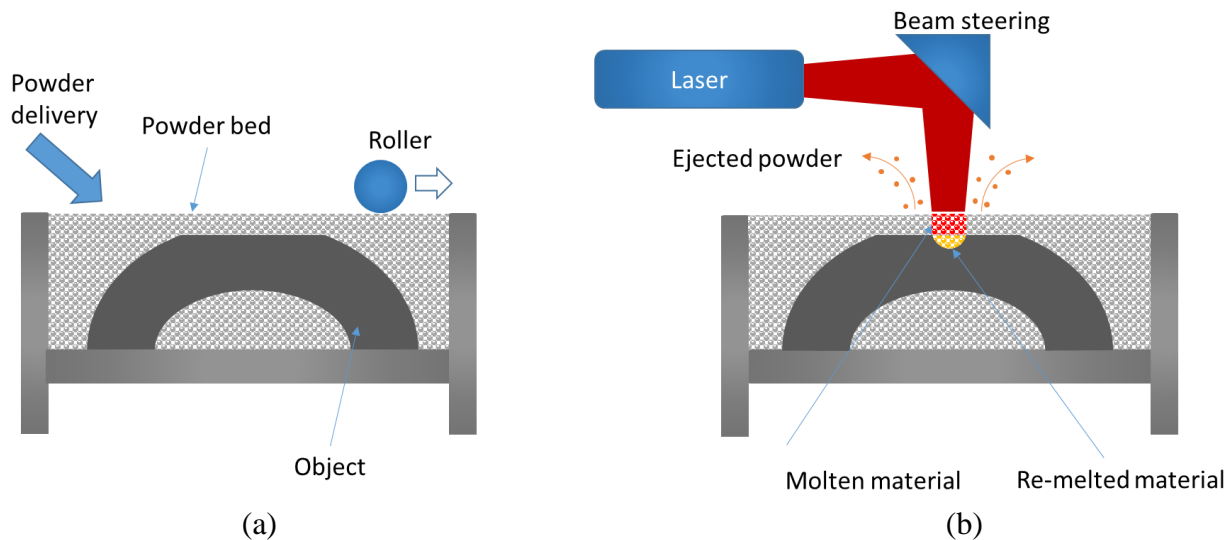
Figure 1 – Overview of SLM: (a) Step 1 prepares the powder bed (b) Fabrication occurs in Step 2 where porosity can be introduced into AM metallic parts due to incomplete melting of powder particles or insufficient overlapping of melt pools

Currently, there exist limited options for nondestructive examination (NDE) of AM structures either during or post-manufacturing. During manufacturing phase, spatial constraints of the 3-D printer limit deployment of many conventional NDE systems, such as radiography. Furthermore, in DLS manufacturing, a metallic part is covered by un-sintered powder. This prevents the use of

contact methods, such as ultrasound, and obscures signals from non-contact methods, such as passive thermography. In post-manufacturing phase, complex shapes composed of planar geometrical primitives with lack of rotational symmetry make it difficult to perform digital radiography. Contact NDE techniques, such ultrasound, would be difficult because AM structures have rough surfaces which affects probe coupling. In addition, NDE methods such as ultrasound and eddy currents require time-consuming point-by-point raster scanning of specimens. As a solution to NDE of AM structures, Argonne is developing pulsed thermal tomography (PTT) models and depth inversion algorithms for 3D imaging and flaw detection. PTT obtains reconstruction of material internal defects by monitoring surface temperature transients following thermal pulse applied to material surface. The method is non-contact, with measurements performed from stand-off distance from one side of the specimen. An imaging camera with megapixel array of detector elements acquires an image of a large section of material. This allows for detection of flaws with minimal amount of mechanical scanning.

A schematic depiction of the PTT setup is shown in Figure 2(a), with the photograph of the laboratory system presented in Figure 2(b). The method consists of illuminating material with white light flash lamp, which rapidly deposits heat on the material surface [10-14]. Heat transfer then takes place from the heated surface to the interior of the sample, resulting in a continuous decrease of the surface temperature. A megapixel fast frame infrared (IR) camera records time-resolved images of surface temperature distribution T(x,y,t). The acquired thermal-imaging data cube therefore consist of a series of 2D images of the sample's surface temperature at consecutive time instants. The unique reconstruction algorithm of PTT developed at Argonne obtains thermal effusivity e(x,y,z) from time-dependent surface temperature T(x,y,t) measurements.

| (a) | (b) |
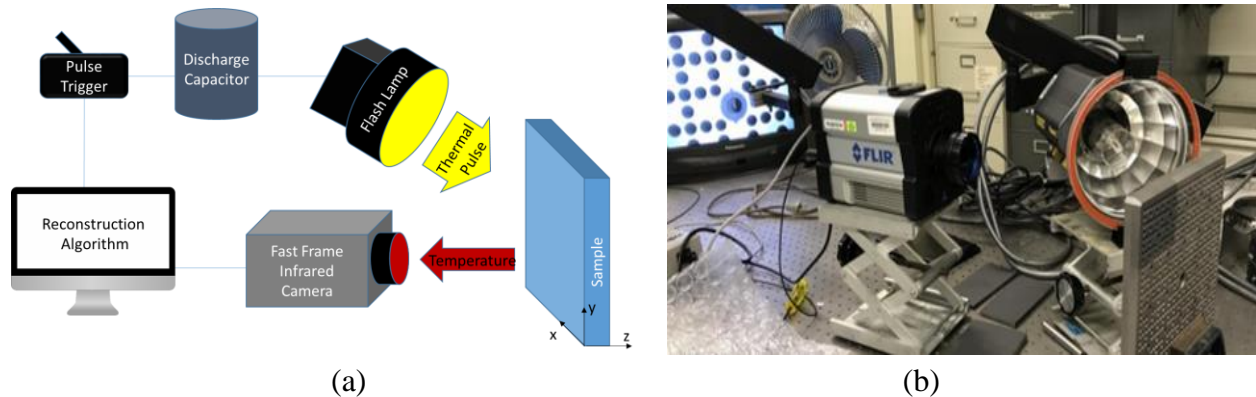
Figure 2 – Principle of pulsed thermal imaging: (a) Schematic drawing (b) Photograph of actual laboratory system

Project objectives addressed in this report include development of performance metrics for PTT detection of flaw size and flaw location relative to material surface. Section 2 described preliminary experimental results of PTT performance evaluation using calibrated defects in high-strength metallic alloys commonly used as reactor structural materials. These include stainless steel 316 and Inconel 718 alloys. Calibrated flaws consisted of cylindrical of variable diameter and

depth imprinted in metallic plates. The results obtained thus far indicate that PTT can image flaws 1mm in size, which is the smallest calibrated flaw created in metallic specimens. Consistent with previous results of the project, results of experiments in Section 3 indicate the general trend in PTT performance that smaller defects can be detected when they are closer to the surface

Section 3 describe the preliminary results of alternative machine learning based analysis of the same data cube analyzed with PTT in Section 2. In this study, an optimized Neural Learning based Blind Source Separation (NLBSS) algorithm, including Principal Component Analysis (PCA), and Independent Component Analysis (ICA) is demonstrated to automatically extract principal temporal and spatial features of thermography frames to enhance flaw detection [15]. Conclusions and brief future work are outlined in Section 4.

2. Pulsed Thermal Tomography Imaging of Calibrated Defects in Additively Manufactured Metallic Specimens

2.1. Development of additively manufactured specimens with imprinted calibrated defects

Calibrated defects developed in this project for evaluation of PTT performance consisted of hemispherical pores imprinted into AM metallic plates. The same pattern of defects was designed for metallic AM stainless steel 316 (SS316) and Inconel 718 (IN718) plates. The plates were produced with the SLM method, and the pores containing un-sintered metallic powder were imprinted into the plates during fabrication. A computer rendering of the pattern of holes is shown in Figure 3.
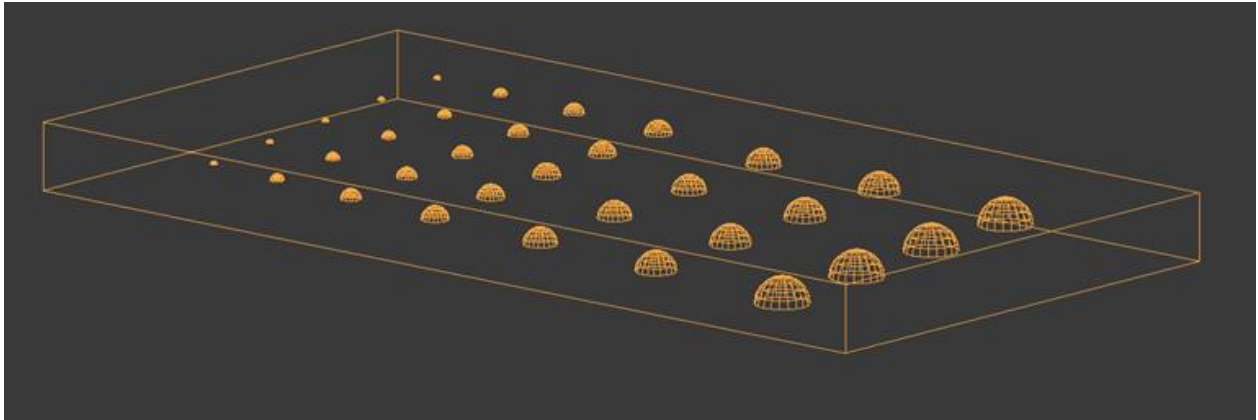
Figure 3 – 3-D rendering of FBH pattern imprinted in AM SS316 and IN718 metallic plates

Figure 4 provides a drawing with labels showing diameters and depths of the holes. Note that there are two patterns of defects on the plate: one with diameters 5,6 and 8mm and depths 2,3,4, and 5mm, and another one with diameters 1,2,3, and 4mm and depths 1,2,3 and 4mm. The holes diameter decreases along the lines parallel to the longer side of the plate, while the depth along each line is held constant. Along the lines parallel to the shorter side of the plate, the depth increases, while the diameter is fixed. The pattern of the defects is the same as that used in a previous study involving simulated flat bottom hole defects (FBH) in SS316 and IN718 plates [10].
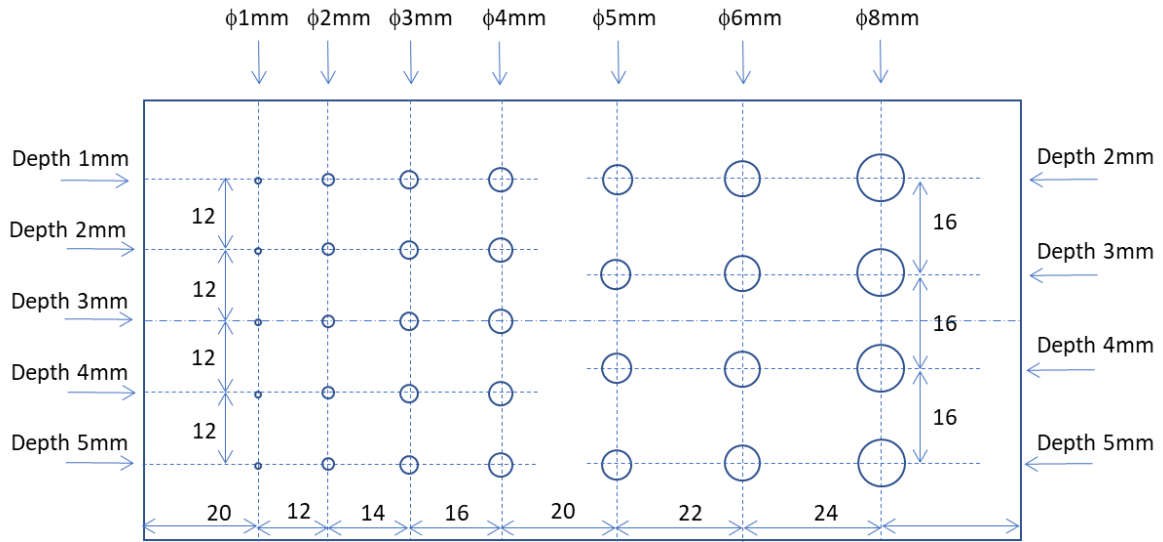
Figure 4 – **Design of hemispherical defetcs of different diameters and depths relative to plate surface**

Figure 5 shows the photograph of two AM SS316 and one IN718 plates. The dimensions of the plates are Length×Width×Thickness: 154 mm × 72 mm × 10 mm. The plates are smooth on both sides.
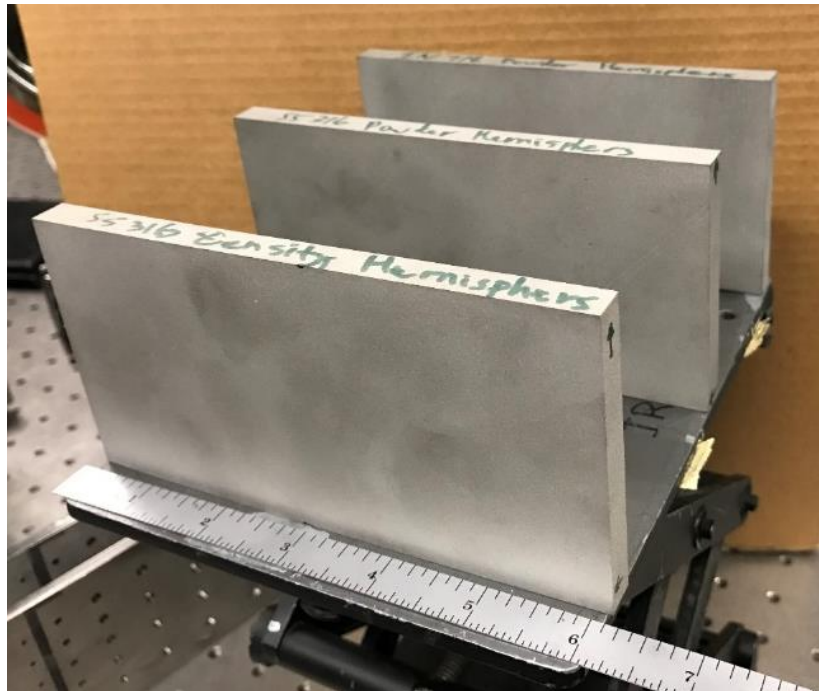
Figure 5 – **Photograph of AM SS316 and IN718 plates**

2.2. PTT imaging of calibrated defects in additively manufactured specimens

The AM metallic plates were imaged with the plates positioned in a way that the spherical side of the internal defects was oriented towards the IR camera. Figure 6 shows the photograph of the setup. For better absorption of thermal energy, all specimens were spay-painted with washable graphite paint. Distribution of incident thermal pulse on the plate is not uniform because the flash light illuminates the metallic plate at an angle. To compensate for this, we have fitted the intensity distribution in the camera frame containing a flash with a polynomial, and then used this polynomial for correction of image intensity in every subsequent frame. The plates were imaged with FLIR X8501sc IR camera with 768x520 pixels window at 216Hz resolution rate. The total imaging time to acquire frames for reconstruction is approximately 8s.
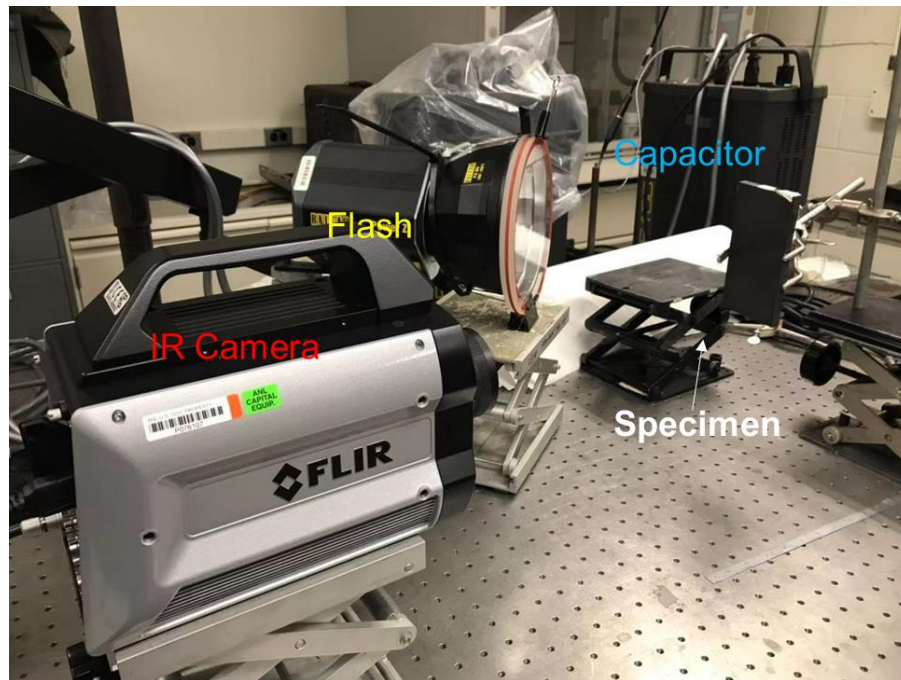
Figure 6 – **Imaging of internal imprinted defects in AM metallic plates**

2.2.1. PTT imaging of Stainless Steel 316 plate with flat bottom holes

Stainless steel 316 (SS316) is frequently used for manufacturing pressure vessel components in light water and advanced reactors because of the alloys high strength and resistance to corrosion. Figure 7 shows reconstructed images of larger FBH at different depths in the material. The left panel of Figure 7 shows the imaged area of the plate. The right panel shows reconstructed parallel plane slices estimated at 2mm, 3mm, 4mm, and 5mm depths. The first column of defects imprinted at 2mm depth and the largest defect at 3mm depth appear in the parallel place slice at 2mm depth. The column of defects imprinted at 2mm and 3mm depth appear in the plane slice reconstructed at 3mm depth. The pattern continues with three and four columns of imprinted appearing in the 4mm and 5mm depth plane slices, respectively. As expected, imaging contrast is better for larger

defects located closer to the surface of the plate. The smallest defect in the imaged plate area with 5mm diameter can be seen as a faint signature in the 5mm depth reconstruction. The reason for appearance of defects imprinted at greater depth in reconstruction planes at shallower depth could be attributed to uncertainty in reconstruction and uncertainty in actual location of the imprinted defect,
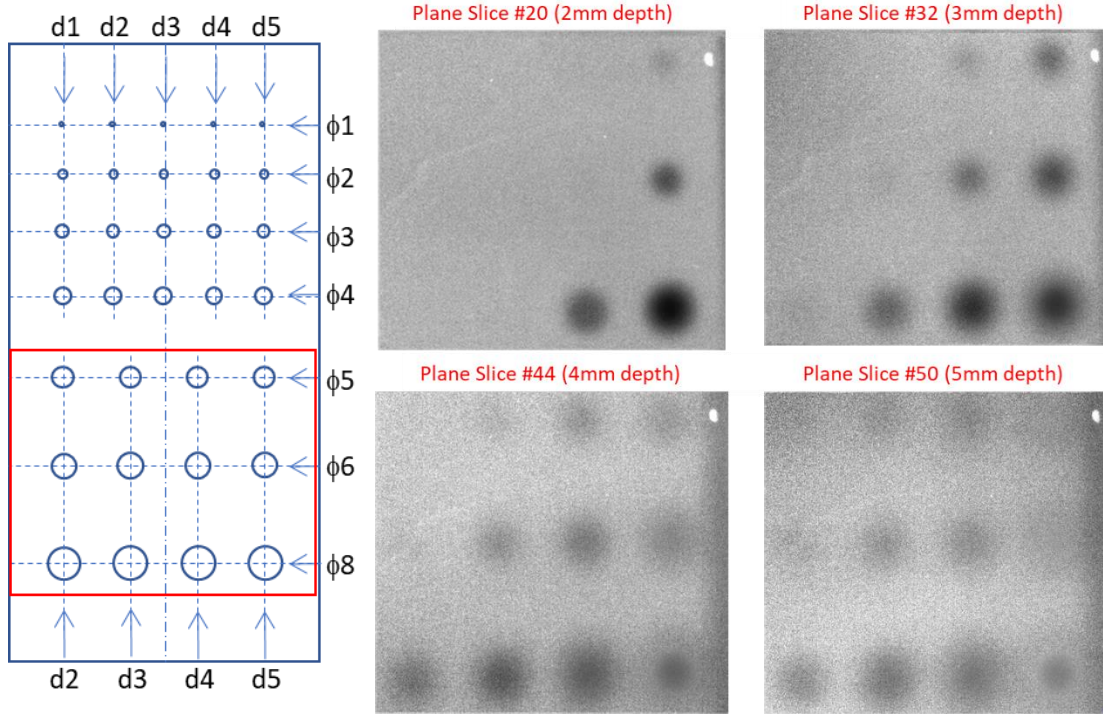
Figure 7 – **Reconstruction of larger defects in SS316 plate. (Left) Imaged area. (Right) Reconstructed parallel plane slices at 2mm, 3mm, 4mm and 5mm depths**

Figure 8 shows reconstructions of parallel plane slices of smaller imprinted defects in the SS316 plate. The left panel of Figure 8 indicates the imaging area of the plate. The right panel of Figure 8 contains reconstructions of parallel plane slices at 1mm, 2mm, 3mm and 4mm depths. All defects down to 1mm size are visible at 1mm depth place slice. At 2mm depth, holes down to 2mm size are clearly visible, and there is a faint signature of the 1mm-diamter defect. At 3mm depth, the smallest visible defect is the 3mm-diameter one. At 4mm depth, the 4mm defect can be detected. Note that these are preliminary qualitative observations. With additional signal processing and thresholding, visibility of smaller size defects might be enhanced.
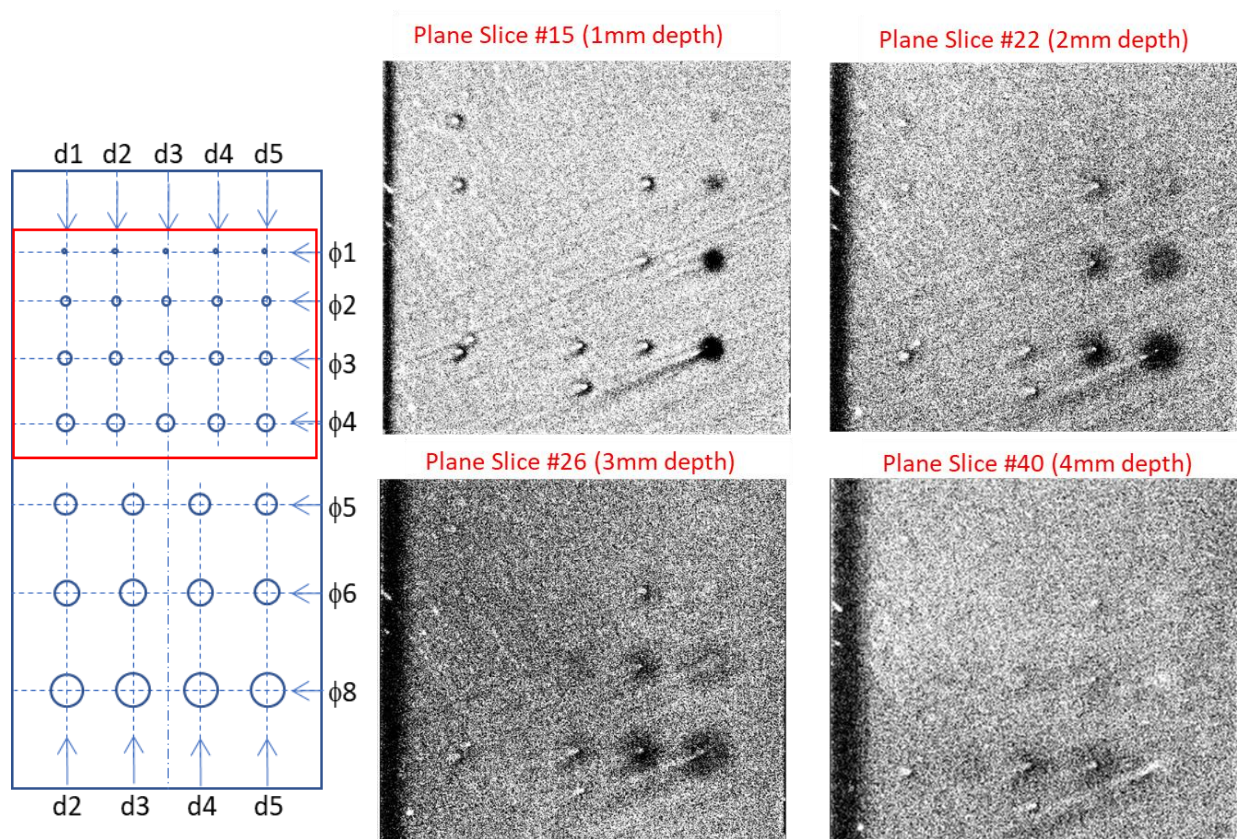
Figure 8 – **Reconstruction of smaller defects in SS316 plate. (Left) imaged area (Right) reconstructed parallel plane slices at 1mm, 2mm, 3mm and 4mm depths**

2.2.2. PTT imaging of Inconel 718 plate with flat bottom holes

Inconel 718 (IN718) is used for manufacturing of components inside the pressure vessel as an alternative to SS316. Parallel plane slice reconstructions of larger defects in the IN718 at various depths are shown in Figure 9. Left panel of Figure 9 shows the imaged area, which consists of larger defects in the IN718 plate. The right panel of Figure 9 shows parallel plane slices at 2mm, 3mm, 4mm, and 5mm depth. The first three reconstructed images show clearly identifiable defects, while the last reconstruction at 5mm depth is becoming difficult to interpret. The smallest defect of 5mm size can be seen in the 5mm depth plane slice.

Figure 9 – **Reconstruction of larger defects in NI718 plate. (Left) Imaged area. (Right) Reconstructed parallel plane slices at 1mm, 2mm, 3mm and 4mm depths**

Figure 10 shows reconstructions of smaller imprinted defects in IN718 plate. The left panel shows the imaged area of the plate. The right panel shows reconstructed parallel plane slices at 1mm, 2mm, 3mm, and 4mm depths. The smallest defect with 1mm diameter is clearly visible in the 1mm depth plane slice. The plane slice at 2mm depth show the first two columns of the defects. The smallest visible defect is the one with 2mm diameter. Reconstruction at 3mm depth shows blurry images of holes, with the smallest defect of 3mm dimeter. The plane reconstructed at 4mm depth shows faint indications of defects with 3mm and 4mm diameters. Overall, the results are similar to PTT reconstructions of the SS316 plate.

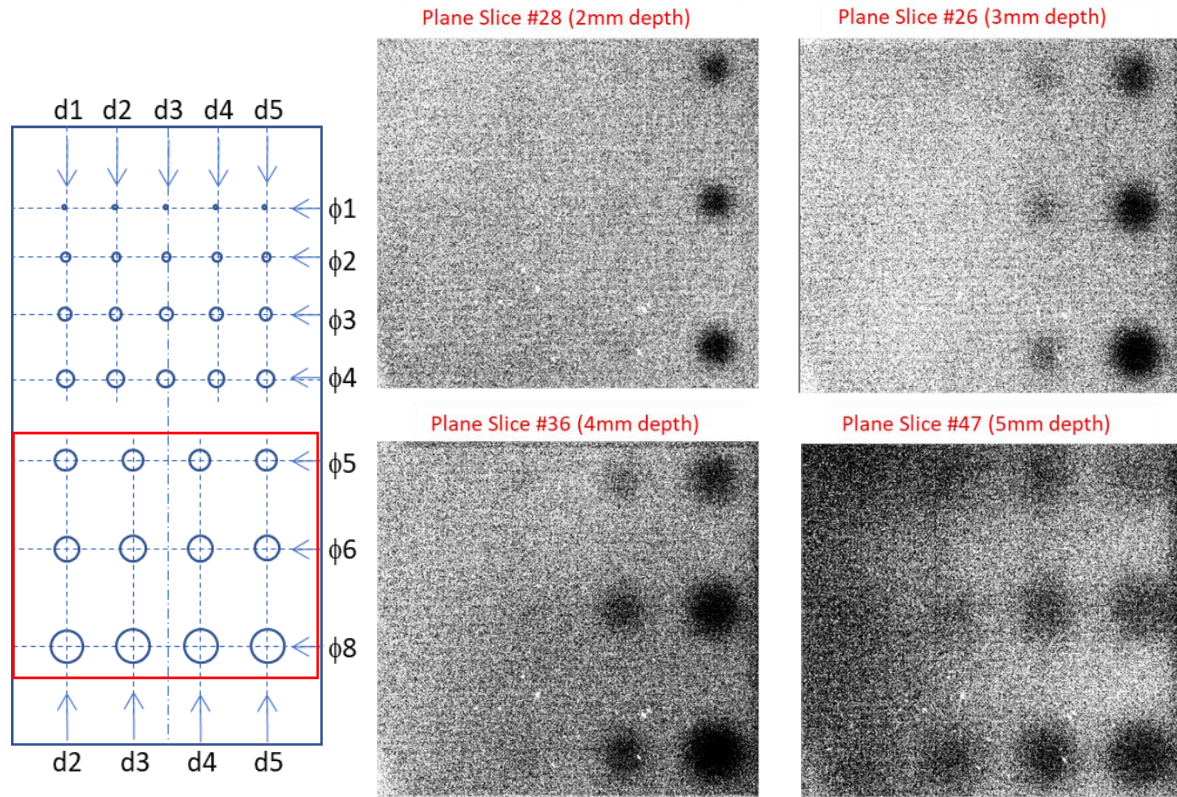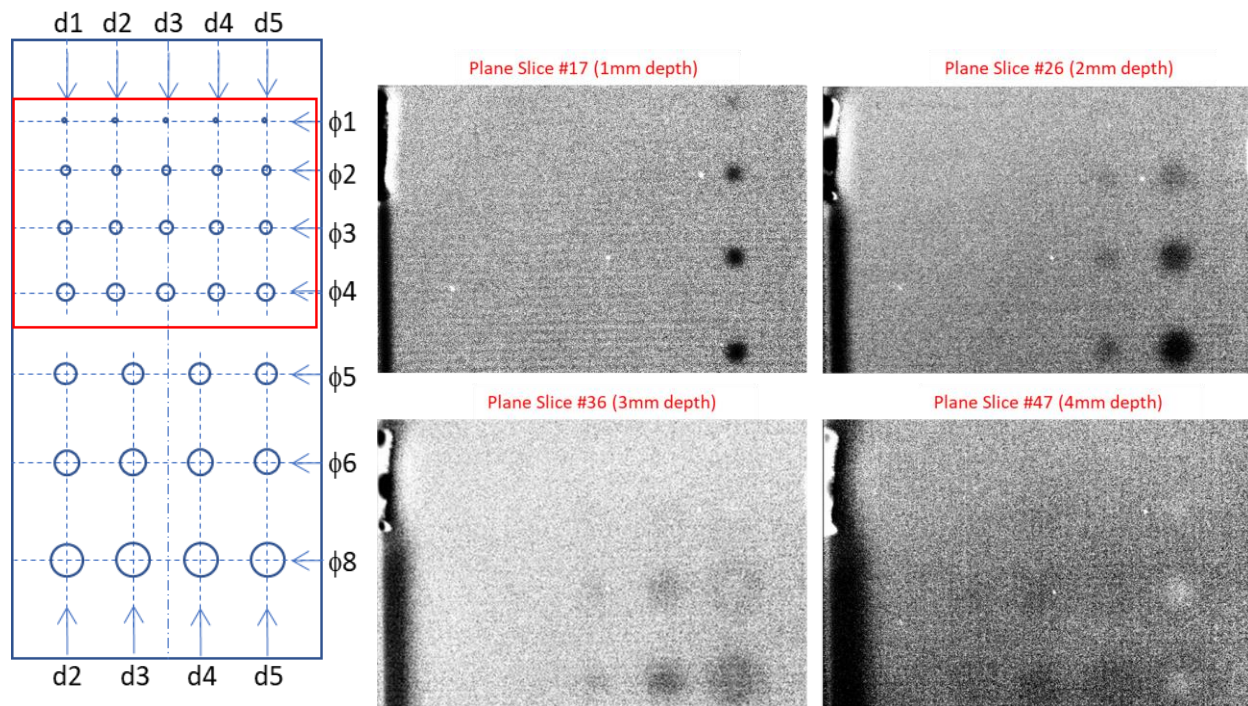**Figure 10** – **Reconstruction of smaller defects in NI718 plate. (Left) Imaged area. (Right) Reconstructed parallel plane slices at 1mm, 2mm, 3mm and 4mm depths**

.

3. Neural Learning Based Blind Source Separation for Detection of Material Defects in Pulsed Thermography Images

Detection of fine features in thermal images is affected by image thermal noise patterns [16], uneven heating of the specimen, and edge blurring. Image processing algorithms should be applied to enhance defect detection efficiency. Traditional image processing methods, such as Gaussian filtering, histogram equalization and sharpening can improve defect detection, but each one is limited to solving a single problem. Recently, algorithms such as Pulsed Phase Thermography (PPT) [17] have been proposed to improve thermal imaging quality. The PPT transforms data from time-domain into frequency spectra using one-dimensional Discrete Fourier Transform (DFT) to extract phase features. The PPT method can reduce the effect of uneven heating but is vulnerable to high-frequency noise [17]. A method called Thermographic Signal Reconstruction (TSR) can robustly increase resolution of thermography frames, enhance visibility of defects in temporal and spatial domain [18]. However, TSR algorithm is inefficient since a very large number of frames need to be analyzed.

We have developed Neural Learning based Blind Source Separation (NLBSS) algorithm, which not only enhances defect detection in time and space, but also automatically separates defects from background and identifies the presence of defects [15]. In NLBSS, we use Principal Component Analysis (PCA) [19] to extract principal features of thermography data, thus reducing thermal imaging noises and artifacts. Next, the Independent Component Analysis (ICA) [20], implemented in a two-layer neural network structure, is applied to automatically separate image regions containing signatures of material defects from image regions which do not contain any material flaws. The neural network structure utilizes the fast fixed-point algorithm for optimization to speed up the defect detection. This approach is computationally simple and requires little memory space. By applying the NLBSS algorithm to experimental thermography data, calibrated subsurface defects of various depths and sizes for the AM metallic material were detected.

3.1. Neural learning based blind source separation

As heat deposited on material surface starts diffusing into the bulk, surface temperature is rapidly decreasing. Material defects, such as pores containing un-sintered powder, have much lower thermal diffusivity compared to solid material. Such material defects are acting as thermal resistances which slow down heat diffusion. This leads to appearance of transient "hot spots" on material surface. These are regions on the surface located above material defects, along the direction of heat diffusion. This concept is further elucidated in Figure 11. The red and green curves show temperatures as functions of time for points in surface regions located above defects and not located above defects, respectively. Temperatures of both points rise rapidly at the same rate during the first second as a result of uniform heat deposition on material surface with a flash lamp. After reaching the maximum at approximately t=1s, both temperatures begin to decay, initially at the same rate. However, after approximately t=2s, the red curve decays at a much slower

rate than the green curve, which gives rise to surface "hot spot." At a given time, the contrast temperature of the "hot spot" can be obtained from the difference between red and green curves. For example, at t=2s, the contrast temperature of the "hot spot" is approximately 3°C. The "hot spot" is visible between t=2s, when the diffusing heat front first encounters the material defect, and t=7s, when material reaches thermal equilibrium. For the temperature values shown in the graphs in Figure 11, the "hot spot" is easily detectable by IR camera with NETD=20mK. However, for smaller material defects, "hot spot" contrast begins to approach the NETD of a camera. Detection of signals close to camera NETD sensitivity threshold, requires image processing to remove noises and experimental artifacts. Therefore, we apply the NLBSS algorithm to enhance defect detection by the independent source signal separation of defects and non-defects regions for flaws detection.
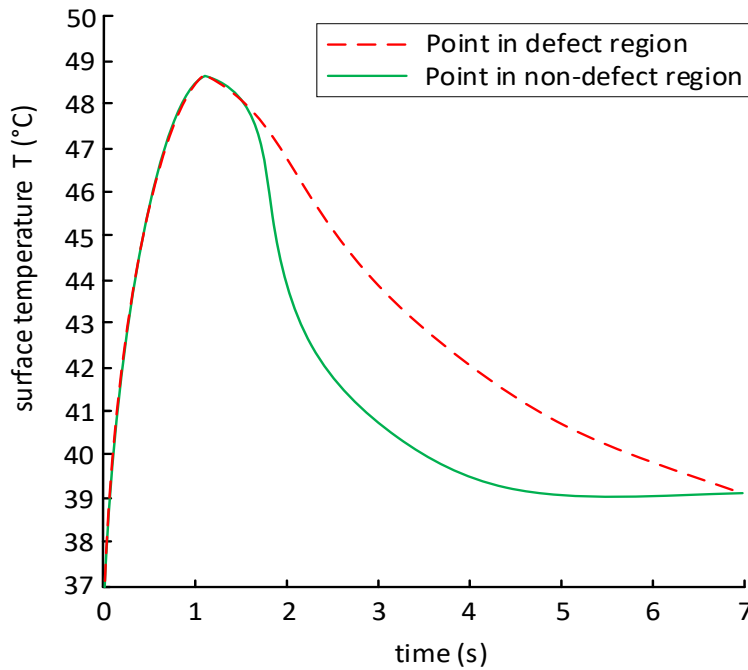
Figure 11 – Surface temperature evolution of points in regions above defect (red) and no-defect (green)

Blind source separation aims at classifying mixed signals into independent source signals without using any a-priori information about the source of signals. In the PT system, the recorded thermography frames (thermograms) are composed of signals from different sources, such as image regions corresponding to defects, regions of no-defects, and noise. Each segment of the thermograms exhibits different temperature evolution during the transient response. In the notation of this paper, each source signal contributes to the Thermal Source Image (TSI). We utilized the NLBSS algorithm to classify TSI and thus to detect defects. The principle of NLBSS is shown in the flowchart in Figure 12.

15
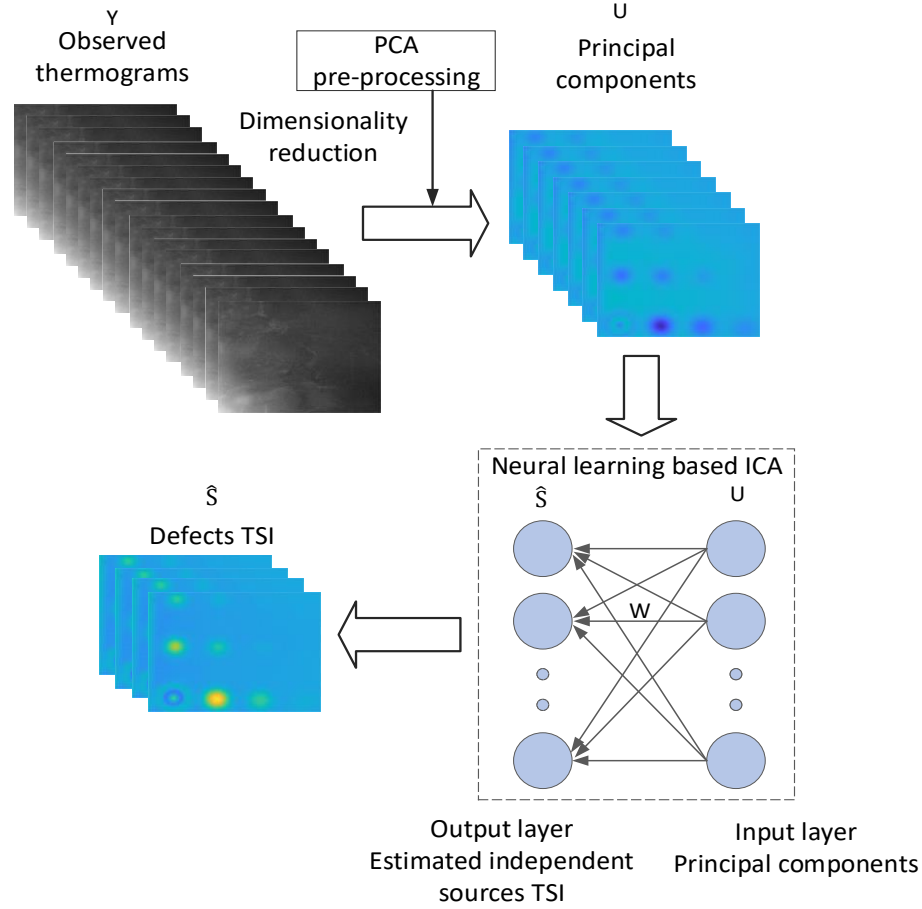
Figure 12 – Flowchart of Neural Learning-based Blind Source Separation algorithm

As shown in Figure 12. The observed thermograms Y are mixed with different source signals that need to be separated. As seen in Figure 12, PCA is used to pre-process thermograms Y to obtain principal components U. Next, the principal components become inputs to the neural learning-based ICA to estimate independent source signals Ŝ, which are TSI's of defects. W is the estimation matrix for separating the mixed thermograms into TSIs of defects. The neural learning-based ICA is implemented in a neural network structure, which is composed of an input layer and an output layer. The principal components of thermograms U form the input layer, and each estimated source signal Ŝ as a neuron forms the output layer. The input layer and output layer are densely connected.

3.1.1. Principal component analysis

We use the Singular Value Decomposition (SVD) to calculate Principal Components (PC). This approach to calculating PC's is faster and suffers less from numerical noise than the more conventional approach based on the covariance matrix. The equation for calculating PC's via singular values is given as:

16

$$Y_{M \times N} = U_{M \times N} R_{N \times N} V_{N \times N}{}^{T} \tag{1}$$

To obtain the PC's of the thermography data-cube matrix using equation (1), we transform the 3D matrix (two spatial and one time axis) into a 2D matrix (one spatial and one time axis) by re-arranging pixels in each thermography frame into a column vector. The dimensions of the condensed 2D matrix Y are M and N, where M is the number of pixels in each thermography frame, and N is the number of recorded thermography frames. U and V are orthogonal matrices separately showing variability of data and time information. R is the matrix containing the singular values of Y. By decomposing the thermography data Y with SVD, matrix U is constructed with principal component analysis (PCA) basis vectors that describe the largest variability in the data using the first few columns (N_I) of U. These PCA basis vectors are decorrelated to enhance the performance of ICA. Thus, we use only few basis vectors of U, which contain principal features of data, as input to ICA estimator for detection of flaws.

3.1.2. Independent component analysis

In the PT system, the surface temperature of each image region corresponding to defect ("hot spot") displays the non-Gaussian distribution during transients. However, the distribution of the sum of N independent source signals approaches Gaussian distribution as N → ∞ regardless of the distribution of each signal [9]. Thus, using the mixed thermography data, which is Gaussian, ICA is applied to obtain a separation matrix W by maximizing the non-Gaussian distribution to detect defects. Equation 2 is used in estimating the TSI of defects $\hat{S}$ to be as close to the original source signal S as possible,

$$\hat{S} = WU^T \approx S \tag{2}$$
$$E\{\hat{S}\hat{S}^T\} = I \tag{3}$$

In equation (2), U is the matrix consisting of principal components of pre-processed thermography data, and W the separation matrix. In order to achieve high efficiency in defects detection, original source signals need to be statistically uncorrelated and non-Gaussian [9]. Thus the estimated TSIs of defects are constrained to be uncorrelated under equation (3). Because we apply the PCA to pre-process the thermography data to be uncorrelated in matrix U, equation (3) is transformed into equation (4) as below:

$$E\{\hat{S}\hat{S}^T\} = WE\{\hat{U}\hat{U}^T\}W^T = WW^T = I \tag{4}$$

In equation (4), the separation matrix W needs to be orthogonal so that the estimated TSIs of defects $\hat{S}$ are uncorrelated. Therefore, we applied the neural learning to implement ICA, and use the fast fixed-point algorithm for optimization to obtain W for defects detection.

The fast fixed-point algorithm is aimed to find a direction to maximize the non-Gaussian properties. In one unit version of this algorithm, to estimate one independent source signal, we need to find a unit vector w_i, so that the projection $w_i^T U^T$ maximizes the non-Gaussian. Here w_i^T is the ith row vector of matrix W. Each unit is optimized as a neuron, which is updated with the

learning rule. For the multi-unit version of this algorithm, multiple output neurons are built to estimate different source signals. Negentropy [20] is approximated to measure the non-Gaussian:

$$O(w) = [E\{G(w^T U^T)\} - E\{G(g)\}]^2 \qquad (5)$$

Equation (5) shows the approximation of negentropy to measure the non-Gaussian as our objective function $O(w)$. G is any nonquadratic function as the contrast function for performance optimization. Here g is the Gaussian variable with zero mean and unit variance. Then, we use the Newton-Raphson Method [21] to iteratively update the unit vector w for maximizing the objective function $O(w)$ under the constraint given in Equation (4). The specific updates and estimate of w can be found in [21]. If the convergence is not satisfied, which means that the old and new values of w still point to different directions, we use the new value of w to initiate another iteration. Otherwise we apply the direction vector w to estimate the independent source signal which, is the TSI of defects in the thermal images.

3.2 Experimental Results

To evaluate performance of the NLBSS algorithm, a thermal pattern graph is constructed to show the estimated TSI of defects. In the experiment, surface regions of defects with similar temperature variation are classified as one TSI. Then, the TSI is highlighted to display defects. In the experiment, the specimen is oriented as shown in Figure 5(a). Two separate experiments were conducted. In one, the lower half of the AM plate was imaged to detect larger defects. In another experiment, the upper half of the AM plate was imaged to detect smaller defects. In each experiment, the camera frame resolution was set to be 576×520 pixels. After thermography frames are acquired by the PC, the NLBSS algorithm is applied to data. We used N = 12 as the number of independent components, which are output neurons, to estimate TSI of defects. The number of principal components was set to $N_1 = 50$ to reduce noise in the images.

3.2.1. Detection of larger defects

PT imaging was performed on the lower half of the AM plate, as indicated with the red box in Figure 13(a). As shown in Figure 13(a), the defects have diameters of 5 mm, 6 mm, 8 mm, and located at depths of 2 mm, 3 mm, 4 mm and 5 mm. An example of a recorded raw image is shown in Figure 13(b). Results of image processing and defect detection using NLBSS algorithm are shown in Figures 13(c) and 13(d). The defects detected in this experiment are indicated with dashed line ovals in Figure 13(a). In particular, Figure 13(c) clearly shows the defect (Ø8,d2), and Figure 5(d) shows the defect (Ø8,d3), defect (Ø8,d4), defect (Ø6,d2), defect (Ø6,d3), and defect (Ø5,d2). The defect (Ø5,d3), defect (Ø6,d4), and defect (Ø8,d5) are detected with relatively lower confidence.
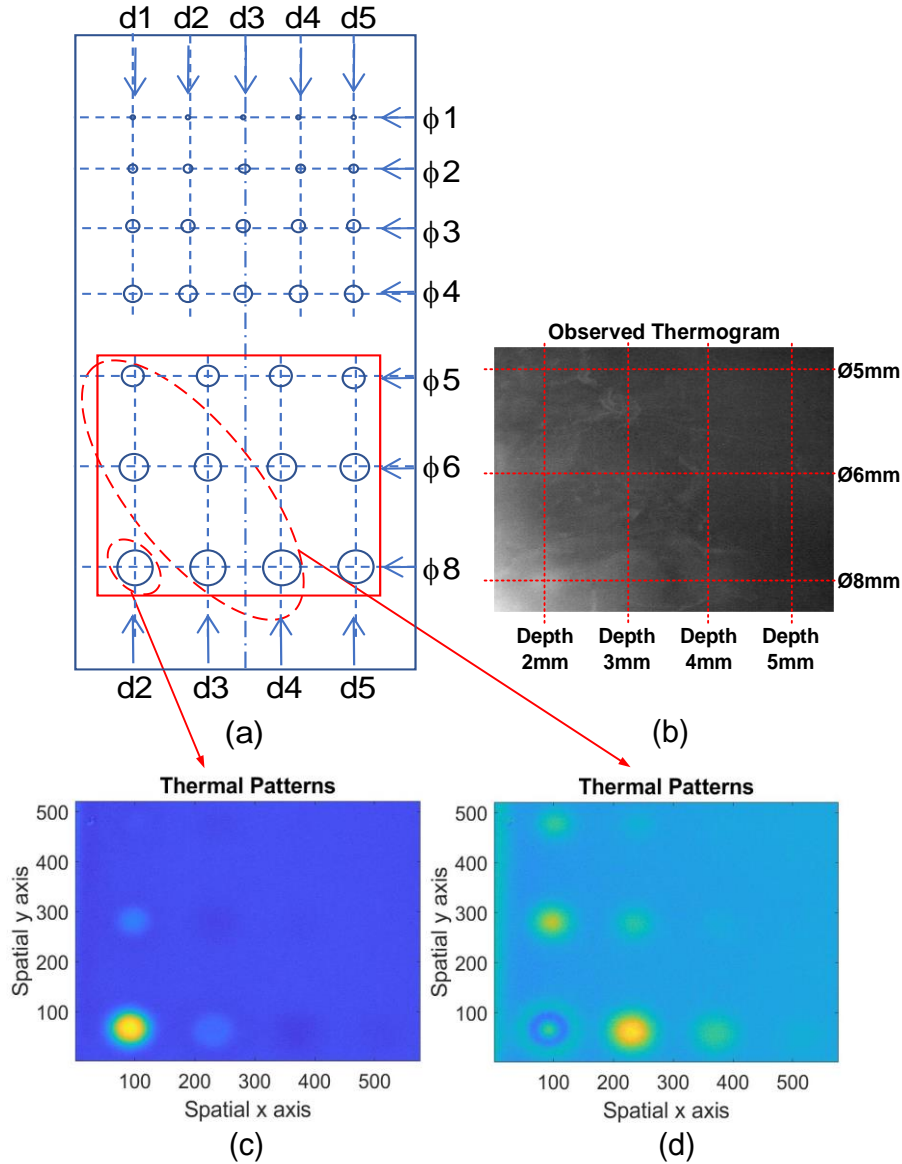
Figure 13 – Detection of larger defects in SS316 specimen

3.2.2. Detection of smaller defects

The experiment was repeated to detect smaller defects in the AM plate. The imaged area of the plate is indicated with a red box in Figure 14(a). Note that Figure 14(a) is Figure 13(a) rotated by 180 degrees. Figure 14(a) shows smaller defects with diameters of 4 mm, 3 mm, 2 mm and 1 mm, and located at depth of 1 mm, 2 mm, 3 mm, 4 mm and 5 mm. Figure 14(b) shows the raw thermogram image recorded with IR camera. After processing the thermograms with the NLBSS algorithm, Figure 14(c) and Figure 14(d) show that the improved detection of defect ($\emptyset 4, d1$), defect ($\emptyset 3, d1$), and defect ($\emptyset 2, d1$), defect ($\emptyset 4, d2$), defect ($\emptyset 3, d2$), and defect ($\emptyset 2, d2$). Detected defects are indicated in Figure 14(a) with dashed line ovals.
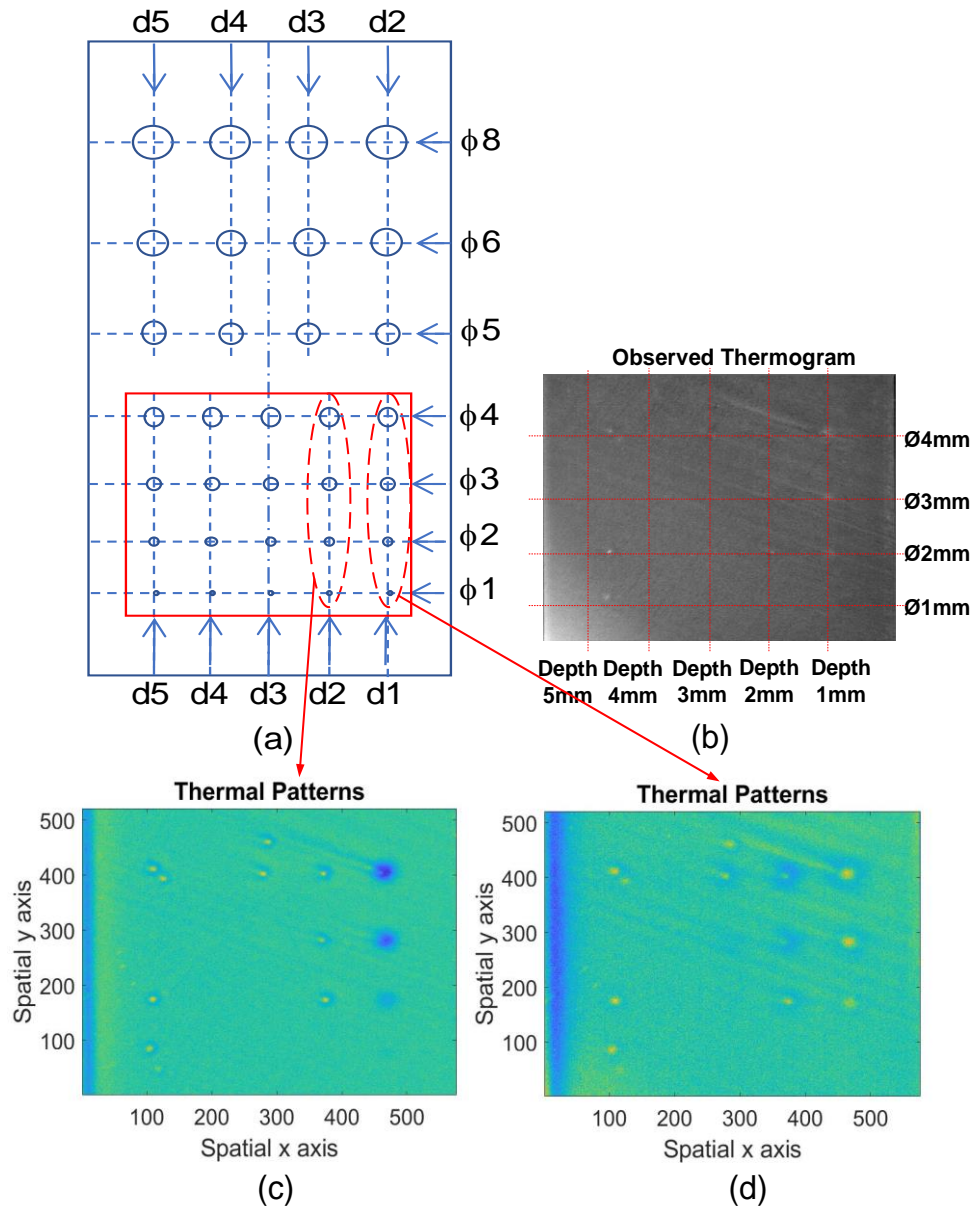
Figure 14 – Detection of smaller defects in SS316 specimen

4. Conclusions

The objective of this report is to provide initial evaluation of pulsed thermal tomography (PTT) performance in detecting calibrated imprinted flaws in AM reactor structural materials. The materials considered in this study included AM stainless steel 316 and Inconel 718 manufactured with SLM. Calibrated defects were created in the form of hemispherical shape pores containing trapped un-sintered powder. Defects were imprinted into metallic plates during fabrication. The diameters of defects varied from 1mm to 8mm, and their depths below the plate flat surface varied between 1mm and 6mm. The sizes of the defects were chosen to be the same as those of the flat bottom hole (FBH) simulated defects in a previous study. PTT imaging results have shown that 1mm-diameter defect located 1mm below the surface in SS316 and IN718 plates were detectable. Larger size defects were detectable at greater depth. For example, 6mm-diameter defect could be detected at 8mm depth. Image contrast was comparable for SS316 and IN718 specimens.

As an alternative approach to analyzing pulsed thermography images to detect internal material flaws, we developed the Neural Learning-based Blind Source Separation algorithm (NLBSS). In the NLBSS algorithm, the Principal Component Analysis (PCA) is applied to pre-process recorded thermograms to enhance defect detection by reducing thermal imaging noise and other experimental artifacts, such as non-uniform illumination of the specimen. Next, Independent Component Analysis (ICA) is used to estimate Thermal Source Images (TSIs) of defects. The ICA is implemented as a two-layer neural network structure, which utilizes the fast fixed-point algorithm for optimization. Our results indicate that internal defects with smaller diameter and deeper location are more difficult to detect. The reason is that defects of smaller size, located farther from the surface have less effect on reducing the heat diffusion, and thus result in low thermal contrast "hot spots" on the specimen surface. Therefore, to further improve the performance of flaws detection, future work will involve optimizing our NLBSS algorithm, such as deploying advanced neural networks as the hidden layers using the transfer learning, to efficiently extract features of thermograms to enhance defect detection.

References

1. G. Bertali, Y. Wang, J. Lim, F. Scenini, C. Long, C, P. Freyer, and M. Burke, "Microstructural Analysis of 3D-Printed Alloy 718," *Microscopy and Microanalysis*, 21(S3), 463-464 (2015).
2. P.D. Freyer, W.T. Cleary, E.M. Ruminski, C.J. Long, P. Xu, "Hot Cell Tensile Testing of Neutron Irradiated Additively Manufactured Type 316L Stainless Steel," *Proceedings of the 18th International Conference on Environmental Degradation of Materials in Nuclear Power Systems -- Water Reactors*: Volume 1, 1021-1038 (2018).
3. R. Cunningham, R., Narra, S. P., Montgomery, C., Beuth, J., & Rollett, A. D. (2017). Synchrotron-based X-ray microtomography characterization of the effect of processing variables on porosity formation in laser power-bed additive manufacturing of Ti-6Al-4V. *JOM*, *69*(3), 479-484.
4. C. Zhao, K. Fezzaa, R.W. Cunningham, H. Wen, F. Carlo, L. Chen, & T. Sun, "Real-time monitoring of laser powder bed fusion process using high-speed X-ray imaging and diffraction," *Scientific Reports, 7*(1), 3602 (2017).
5. K. Kempen, E. Yasa, L. Thijs, J.P. Kruth, & J. Van Humbeeck, "Microstructure and mechanical properties of Selective Laser Melted 18Ni-300 steel," *Physics Procedia*, *12*, 255-263 (2011).
6. W.J. Sames, F.A. List, S. Pannala, R.R. Dehoff, & S.S. Babu, "The metallurgy and processing science of metal additive manufacturing," *International Materials Reviews*, 61(5), 315-360 (2016).
7. J.J. Lewandowski, & M. Seifi, "Metal additive manufacturing: a review of mechanical properties" *Annual Review of Materials Research*, *46*, 151-186 (2016).
8. A. Heifetz, D. Lisowski, M. Weathered, Y. Momozaki, H.T. Chien, S. Bakhtiari, "Preliminary Review Analysis of Distributed Sensors for Versatile Test Reactor (VTR) Environment," Argonne National Laboratory, ANL/NSE-18/11 (2018).
9. M. Wakamatsu, H. Nei, and K. Hashiguchi, "Attenuation of temperature fluctuations in thermal striping," *J. Nucl. Sci. Technol.*, vol. 32, no. 8, pp. 752–762 (1995).
10. A. Heifetz, T. W. Elmer, J. G. Sun, T. Liu, D. Shribak, B. Saboriendo, S. Bakhtiari, X. Zhang, J. Saniie "First Annual Report on Pulsed Thermal Tomography Nondestructive Evaluation of Additively Manufactured Reactor Materials and Components," Argonne National Laboratory ANL-19/43 (2019).
11. A Heifetz, D. Shribak, T. Liu, T.W. Elmer, P. Kozak, S. Bakhtiari, B. Khaykovich, W. Cleary, "Pulsed Thermal Tomography Nondestructive Evaluation of Additively Manufactured Reactor Structural Materials," *Transactions of the American Nuclear Society* 121(1), 589-591 (2019).
12. A. Heifetz, J.G. Sun, T.W. Elmer, D. Shribak, B. Saboriendo, P. Kozak, S. Bakhtiari, W. Cleary, B. Khaykovich, "PTT System Performance Evaluation in 3-D Imaging of Calibrated Defects," Argonne National Laboratory, ANL-19/12 (2019).
13. A. Heifetz, T. Liu, D. Shribak, "PTT System Design and Data Analysis for Improved Performance," Argonne National Laboratory, ANL-19/25 (2019).
14. A. Heifetz, T.W. Elmer, X. Zhang, J. Saniie, "PTT System Performance Evaluation in 3-D Imaging of AM Components," Argonne National Laboratory ANL-19/38 (2019).

15. X. Zhang, J. Saniie, A. Heifetz, "Neural Learning Based Blind Source Separation for Detection of Material Defects in Pulsed Thermography Images," submitted to *IEEE International Conference on Electro-Information Conference (EIT)*, May 2020.
16. C. Ibarra-Castanedo, A. Bendada and X. Maldague, "Thermographic image processing for NDT," *IV Conferencia Panamericana de END* (2007).
17. E. D'Accardi, F. Palano, R. Tamborrino, D. Palumbo, A. Tatì, R. Terzi, U. Galietti, "Pulsed Phase Thermography Approach for the Characterization of Delaminations in CFRP and Comparison to Phased Array Ultrasonic Testing," *Journal of Nondestructive Evaluation* 38:20 (2019).
18. S.M. Shepard and M. Frendberg Beemer "Advances in thermographic signal reconstruction," *Proc. SPIE* 9485, *Thermosense: Thermal Infrared Applications XXXVII* (2015).
19. X. Zhang, T. Gonnot, J. Saniie, "Real-Time Face Detection and Recognition in Complex Background," *Journal of Signal and Information Processing*, Volume 8, 99-112 (2017).
20. A. Hyvärinen. "The Fixed-Point Algorithm and Maximum Likelihood Estimation for Independent Component Analysis," *J. Neural Processing Letters*, Volume 10, Issue 1, pp 1–5 (1999).
21. S. Akram and Q. ul Ann, "Newton Raphson Method," *International Journal of Scientific & Engineering Research*, Volume 6, Issue 7, 1748-1752 (2015).

Nuclear Science and Engineering (NSE) Division
Argonne National Laboratory
9700 South Cass Avenue, Bldg. 208
Argonne, IL 60439

www.anl.gov